Energy 313 (2024) 133765

Contents lists available at ScienceDirect

Energy

journal homepage: www.elsevier.com/locate/energy

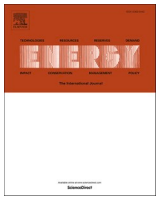

Evaporation and combustion of low asphaltene heavy oil droplets under conditions representative of practical applications

Taha Poonawala, Alvaro Muelas *, Javier Ballester

Laboratory of Fluids Engineering and Energy (LIFEn), Engineering Research Institute of Aragon (I3A), University of Zaragoza, 50018, Zaragoza, Spain

ARTICLE INFO

Keywords:
Heavy oil
Droplet evaporation
Droplet combustion
Cenosphere combustion
Flame-like conditions
Micro-explosions

ABSTRACT

The evaporation and burning characteristics of isolated heavy fuel oil (HFO) droplets are experimentally studied at conditions representative of practical applications, producing novel, detailed results on the effect of oxygen concentration. Also, and for the first time for HFO, the temporal evolution of the flame stand-off ratio (based on CH* emission) and the cenosphere burning size are presented along with the droplet size histories. The effect of ambient oxygen concentration is first analyzed qualitatively, identifying different sub-stages. Later, a quantitative analysis is presented in terms of ignition delay time, micro-explosion regimes, shell swelling ratio, cenosphere size and several time metrics. The results show that, as ambient oxygen changes, the liquid and solid stages show marked differences not only in terms of time scales but also in the transition of burning regimes. Cenospheres generated in oxygen-free conditions are found to be ~1.4 times larger than those in droplet combustion. Although similar in size, the solid-to-liquid consumption time ratio in 5% O_2 is found to be significantly longer, about twice than for the 10% O_2 ambient. The characterization of these differences is thought to be relevant not only for oil flames but also for the promising future of heavy oil gasification applications.

1. Introduction

Due to recent developments and regulations, different technologies are continuously evolving to achieve a cleaner and more efficient utilization of heavy fuel oil (HFO) and other petroleum residues. Various strategies such as blended heavy-oil combustion in internal combustion engines [1], fuel flexible firing in a dry low NOx gas turbine engine [2], chemical-looping combustion [3] as well as gasification technology [4] are being applied, to name a few. Furthermore, the combustion and gasification of alternative liquid fuels such as residual, pyrolysis and slurry oils (e.g. vacuum residue oil, tire pyrolysis oil, etc.) are under active consideration by researchers due to their high waste-to-wealth value [5,6]. Resembling HFO, some of these fuels are also viscous, not so equipment-friendly and exhibit complex evaporation and combustion characteristics such as disruptive evaporation (droplet micro-explosions), solid residue generation, longer ignition delay times, etc. [7]. Therefore, in this scenario of future interest and the associated challenges with such difficult-to-burn (DTB) liquid fuels/oils, HFO is chosen for detailed studies in the present work due to its intrinsic relevance as well as a representative of DTB liquids.

Irrespective of its final application (combustion or gasification), heavy fuel oil is usually injected as a dense spray of fine droplets (50–100 μm [8–10]) and hence, isolated droplet methods have been widely employed for its detailed characterization. For this, two main configurations are available viz., free falling type and suspended droplet type. The first kind has been traditionally preferred for coke (cenosphere) formation studies [11–16], whereas suspended droplets have been used more often for the intrinsic characterization of the liquid phase [11,17–24], as well as for cenosphere morphology [15,16,25,26] or even the interaction between both [27]. A common key finding from these studies is that the combustion of every droplet of heavy oil consists of three basic processes: liquid phase evaporation, generation of cenosphere and, for cases with ambient temperature >1150 K [25] and enough O_2 availability, the burning of the cenosphere. The

* Corresponding author. Laboratory of Fluids Engineering and Energy (LIFEn) Engineering Research Institute of Aragon (I3A), University of Zaragoza Calle Maria de Luna, 10, 50018 Zaragoza, Spain.
E-mail address: amuelas@unizar.es (A. Muelas).

https://doi.org/10.1016/j.energy.2024.133765
Received 16 July 2024; Received in revised form 25 September 2024; Accepted 7 November 2024
Available online 7 November 2024

polymerization of HFO heavy compounds is reported to form a viscous shell which condenses into a solid cenosphere [12,16,24,26], whose properties vary with the fuel and the particular conditions. For cases where the cenosphere burns, it occurs in stages such as glowing delay, oxidation and burnout with fragmentation, being the solid-to-liquid burning time ratio in hot ambient air (21% O_2) of the order of 1.3–2 [23,25]. Thus, the burning of the solid residue becomes a limiting factor for achieving a complete conversion of HFO droplets within a given residence time.

While previous studies have greatly contributed to the current understanding of HFO droplet combustion, it is interesting to note that most works have utilized the suspended droplet technique with closely similar test conditions, as summarized in Table 1. With the exception of the pioneering work of Hottel et al. [28] and few quantitative results from suspended tests by Marrone et al. [11], practically all such studies had the droplet surrounded by 21% O_2 (i.e. fresh air), while also using relevant but relatively low gas temperatures. However, the detailed measurements of temperature and species concentration inside real flames of heavy oil show that most of the injected fuel droplets evaporate/burn at 0–5% O_2 and very high temperatures, ~1700 K [29]. Moreover, the cenospheres generated in practical applications would be consumed downstream of the flame, where low oxygen conditions are bound to exist [29], with temperatures of ~1400 K (a limit imposed by the material in common use for the heat/work transfer equipment). Furthermore, despite the clear interest and relevancy of heavy fuel oil gasification [4], only a handful of detailed results are available, e.g. see Refs. [30–34]. These studies suggest that a minimum temperature of 1100 K along with steam/O_2 as gasifying agents is required for better quality of syngas [33] as well as to utilize Entrained Flow Gasifiers (EFGs) which operate at ~1700 K for obtaining tar-free syngas [35]. Thus, despite the obvious differences in ambient composition due to the presence of steam/gasifying agents, experiments on single droplets at high temperatures and low/zero oxygen concentration can be also clearly relevant for HFO gasification.

In this context of conditions encountered in practical applications compared to the experimental conditions tested so far, the authors note the following: (1) heavy oil behavior (qualitatively and quantitatively) will vary with ambient %O_2, but surprisingly there are no results on this (except those presented but not discussed in Refs. [11,28]), (2) the majority of heavy oil droplets usually evaporate inside the spray core (in combustion as well as in gasification applications) and hence its characterization under O_2-free and low O_2 atmosphere is needed and clearly lacking, (3) despite the great practical relevance of cenosphere burning for the design and sizing of HFO combustion equipment, the most relevant experimental results have been presented in terms of burning times for identified regimes based on visual appearances in Refs. [20,22,23] whereas the temporal evolution of cenosphere size during its consumption has not been reported so far, and (4) some characterization methods that have become standard for detailed studies of droplet combustion and validation of numerical models, (e.g. the identification of the diffusion flame surrounding evaporating droplets based on radicals) have barely been applied to the case of HFO; (5) furthermore, in the few studies where the droplet envelope flame has been characterized [15,24], its visualization and subsequent quantification has been based on the black-body emission of soot particles, rather than on chemiluminescent emission commonly used to detect the actual reaction zone. Therefore, despite the abundant literature on HFO combustion, it can be concluded that all these aspects represent relevant research gaps that need to be addressed to achieve a detailed description of the main droplet behaviors and underlying mechanisms and cover conditions (in terms of temperature and oxygen concentration ranges) representative of high-temperature HFO gasification and combustion applications.

Accordingly, the present work is aimed at bridging these existing research gaps. To that end, evaporation and combustion of HFO droplets have been studied under conditions representative of practical applications, significantly extending the ranges normally found in the literature. The suspended droplet technique has been adopted in this study, as it allows to follow the whole evaporation/burning history of a single droplet. A potential drawback, however, is that this configuration is known to be susceptible to various undesired effects viz., fiber conduction, radiative heat absorption and forced/natural convective heat transfer [36]. Taking care of these aspects, a suspended droplet facility has been developed, providing ambient conditions that differ from those reported so far (as compared in Table 1), while also keeping the transport field close to the canonical, 1-D case. Novel results in terms of chemiluminescence-based flame stand-off ratio, liquid droplet size evolution and cenosphere burning history are presented first in section 3.1. Later in section 3.2, the effect of ambient oxygen concentration is specifically quantified and discussed in terms of ignition delay time, micro-explosion regimes, shell swelling ratio, cenosphere size and time metrics.

Table 1
Comparison of common test conditions in the literature with those employed in the present work for tests with suspended droplets of heavy oil.

Parameter	Conditions tested	Present work
Initial droplet size	≈0.5–2 mm	≈0.5 mm
Ambient temperature	≈700–1200 K	• 1336 ± 50 K for pure evaporation • 1408 ± 20 K for cenosphere combustion
Ambient %O_2	≈21% in most cases	0%, 5% and 10%
Ambient convective field	Quiescent (e.g. V_g ~0–0.08 m/s), or forced (e.g. V_g ~7 m/s)	$Re \approx O(0.5)$ based on droplet diameter
Radiative heat flux	Not quantified, but usually it is a relevant heat source (e.g. furnace walls, flames, heating elements, etc.)	23.5 kW/m^2 (weak)
Fiber diameter	≈100–200 μm (thick)	15 ± 3.75 μm (thin)
Fiber type	S-type thermocouple (Pt/Pt13Rh, k_{fiber} = 80 W/(m·K)) or quartz (k_{fiber} = 1.4 W/(m·K))	Nicalon™ SiC (k_{fiber} = 2 W/(m·K))

2. Experimental methodology

2.1. Fuel properties

In this work, an industrially sourced sample of heavy fuel oil is studied. The physical properties and the chemical composition of the sample are given in Table 2.

Table 2
Properties of the heavy oil used in the current work.

Parameter	Value	Test Method
Density at 25 °C (kg/m^3)	971	ASTM D1480-21
Asphaltene (n-C5) (%wt.)	5.28	ASTM D2007-19
Higher heating value (MJ/kg)	43.028	UNE 164001 EX
Ultimate analysis (%wt.)		UNE-EN 5104
C	88.30	
H	10.61	
N	1.02	
S	0.69	

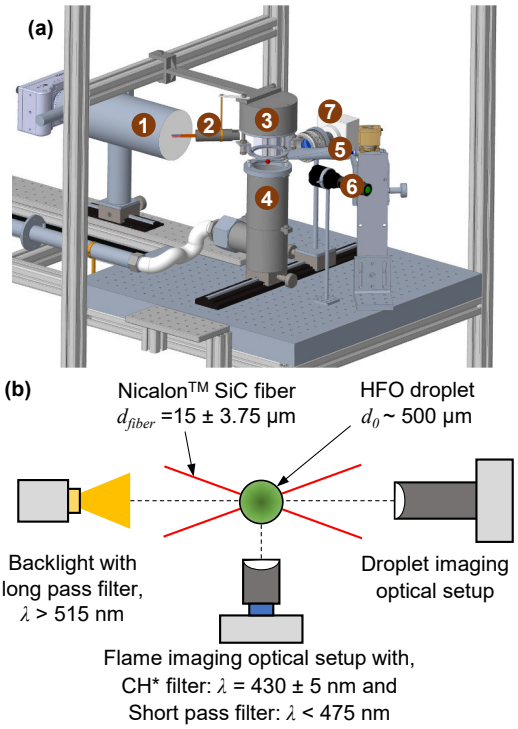

Fig. 1. Suspended droplet facility (a) 3D view: 1-droplet imaging optical setup, 2-flame detector, 3-McKenna flat flame burner, 4-droplet holder assembly, 5-air shield with solenoid valve, 6-backlight for droplet imaging, 7-flame imaging optical setup; (b) Schematic top view.

2.2. Suspended droplet facility (SDF)

Fig. 1(a) shows a 3D view of the developed facility with all its components. The droplets evaporate/burn in a high temperature stream of combustion products generated by a McKenna flat flame burner. The burner operates with premixed CH_4/Air/O_2 so that the %O_2 in the flue gases can be adjusted as required. To achieve an oxygen-free ambient, the flow rates of CH_4/Air are fixed at slightly rich conditions ($\varphi = 1.07$), with 94 Nl/h of methane and 835 Nl/h of air. Similarly, for attaining 5 and 10% O_2 by volume in the hot co-flow, an additional stream of pure O_2 (50 and 100 Nl/h) was added to this fixed premixture of CH_4/Air. The burner's combustion products (consisting mainly of N_2, H_2O, CO_2 and, for some cases, O_2) are confined by a quartz tube, supported at the base of the McKenna burner and vertically oriented, with the flow moving downwards. The H_2O/O_2 mass fraction ratios for combustion conditions are estimated to be 2.88 and 1.22 for the co-flow containing 5 and 10% O_2, respectively. At the outlet of the quartz tube, a sufficiently wide and thin nozzle creates a horizontal jet of cold air that prevents the hot gases from reaching the droplet until the test is started (see element #5 in Fig. 1(a)). The droplet is deployed at the intersection of two 15 µm Nicalon™ SiC fibers placed in a cross-fiber arrangement (Fig. 1(b)) and supported by a holder ring. This droplet holder assembly is mounted on a manual rack-pinion traverse so that, during the test, it can be positioned coaxially under the McKenna burner and the quartz tube confining its combustion products. An extraction system is installed underneath this assembly to evacuate the downward hot gas flow and to maintain its uniformity and laminarity.

To record the full temporal evolution of the isolated suspended droplet, two optical setups are placed perpendicularly to minimize any interference between each other. These are shown schematically in Fig. 1(b). The first optical setup aims to record the droplet evolution with a high temporal resolution. For this, a long-distance microscopic lens (Questar QM1) is mounted on a Chronos 2.1-HD camera that can record up to 24,000 fps. For the present case, a resolution of 1024 x 768 pixels and an exposure time of 100 µs were fixed, with two different frame rates depending on the purpose of the test. For tests where the liquid consumption (i.e. until cenosphere is formed) is of interest, a frame rate of 2500 fps has been used, whereas for recording the total droplet burning sequence (i.e. until the cenosphere burns completely), a lower frame rate of 500 fps has been applied. This is a reasonable choice since coke burning time scales are significantly longer than liquid consumption times [20,23]. To enhance the droplet contour sharpness, a strong backlight is installed with a 515 nm long-pass filter to avoid interference with the second setup, which records the weak bluish flames. The spatial resolution of this optical setup is 3.432 ± 0.05 µm/px. A sample image captured by this setup is shown in Fig. 2(a), where a heavy oil droplet and the surrounding soot particles can be observed.

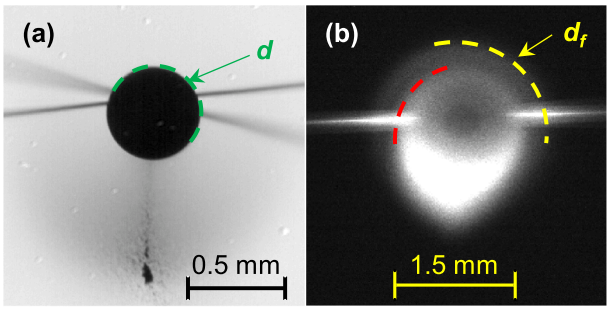

Fig. 2. Sample images of: (a) heavy oil droplet and (b) the corresponding envelope flame simultaneously captured by the respective optical setups. The instance shown is 45 ms after ignition of a droplet with $d_0 = 462$ µm in a 10% O_2 condition. The red and yellow boundaries shown in (b) indicate the emission from the inner soot cloud and the actual diffusion flame (CH* chemiluminescence), respectively. (For interpretation of the references to colour in this figure legend, the reader is referred to the Web version of this article.)

The second optical setup aims to simultaneously record images of the diffusion flame formed around the droplet. A high-sensitivity, monochrome Hamamatsu Orca C11440-36U camera is used along with a Nikkor 50 mm f/1.4 lens and a CH* narrow bandpass filter (430 ± 5 nm, OD 4) to capture the flame reaction zone, as identified by chemiluminescent emission due to this radical [37]. To further eliminate the much stronger black-body emission of soot particles, a short-pass filter ($\lambda <$ 475 nm, OD 4) is also added. For the present case, a resolution of 800 x 960 pixels has been used with an exposure time of 15 ms and a frame rate of 66 fps. This configuration is adequate to capture the weak chemiluminescence of the envelope flames with a quite high signal-to-noise ratio, as it can be assessed from the sample image provided in Fig. 2(b). This setup was calibrated to achieve a spatial resolution of 12.465 ± 0.06 µm/px. Interestingly, the use of two complementing filters reduces the very strong emission of inner radiating soot cloud and establishes a clear distinction for the outer blue flame, thereby allowing to measure the actual CH*-based flame diameter, which to the authors' knowledge, is extracted for the first time for heavy oil droplets.

Every test sequence comprises several steps and triggering events, synchronized using Arduino Mega 2560, with an interface developed in MATLAB®. First, the cold air jet shield is turned on. Thereafter, a ~500 µm droplet is deployed at the intersection of the two crossed SiC fibers by using a 90 µm tungsten wire. Even if clearly above droplet sizes in typical sprays, using this initial droplet diameter is considered as a good compromise between experimental accuracy and a reasonably closeness to realistic sizes. For ease of deployment, the viscosity of heavy oil was decreased by keeping it in a hot water bath at 40–50 °C. Once the droplet is placed on the fibers, the droplet holder assembly is traversed to its final position, triggering a timing event. This starts the image acquisition by both cameras and closes afterwards the solenoid valve of the air shield, leading to a sudden rise in temperature at the droplet location,

thereby causing the droplet to evaporate/burn. Sequentially, 5 repeated tests were conducted to characterize the evolution of the liquid droplet for each condition, whereas 7–8 repetitions were performed for the consumption of the solid cenosphere under oxidizing atmospheres (5–10% O_2, respectively). Differences in d_0 within each test group were minimized, so that relative standard deviations for d_0 lie between 5.7 and 13.7%. Finally, the acquired droplet and flame images were processed using a MATLAB® algorithm whose details are given in the supplementary materials (appendices A and B, respectively).

Ambient conditions at the droplet location are characterized in terms of gas temperature, composition, velocity and radiative heat flux. For measuring the gas temperature, a 75 μm, bare-wire S-type thermocouple was used. The results show that, under cold conditions (i.e. while the air shield is operating) the ambient temperature is 325 ± 1 K. After the closure of the air shield, the temperature rapidly increases, reaching a value of 1336 ± 50 K during droplet evaporation (at 0% O_2 in co-flow). This temperature range is estimated by considering typical liquid consumption times. Shortly after, the temperature stabilizes at a steady value of 1408 ± 20 K. Due to the much longer conversion times for the cenospheres (as it will be detailed further on), this is considered as the average ambient temperature during cenosphere combustion. Local measurements over a domain of ±5 mm around the droplet location (~$10d_0$), indicate a uniform temperature field, within ±10 K. Temperature was also measured at 5% and 10% O_2 conditions, yielding very similar values. The co-flow gas composition was measured with a Testo-350 analyzer which confirmed the %O_2 (by vol., dry basis) in the co-flow for the set mixture flow rates. An ellipsoidal radiometer measured the radiative heat flux at the droplet location as 23.5 kW/m^2. Gas velocity was estimated by processing the traces of trailing soot particles (as seen in Fig. 2(a)) with the Open PIV [38] software in MATLAB®. The resulting gas velocity is of the order of 0.1 m/s, which corresponds to droplet Reynolds number ~0.5 during its lifetime. As a further experimental evidence, the envelope diffusion flames obtained for a non-sooty pure compound such as 1-pentanol exhibited good sphericity (see appendix B, Fig. B.1), thus confirming negligible effects of forced convection and buoyancy. For this specific combination of experimental conditions (thin, low-conductive fibers: d_{fiber} = 15 μm, k_{fiber} = 2 W/(m·K)), small droplets ($d_0 \approx$ 500 μm), weak radiative heat flux (Q_r = 23.5 kW/m^2) and a weak convective field with Re ≈ O(0.5), the evaluation of experimental artifacts as given in Ref. [36], results in $(FN + RN + CN) \sim 0.2$. This corresponds to an experimental deviation in terms of quasi-steady evaporation rate of the order of 10% [36] when compared to an ideal, canonical case, which is about the lowest deviation attainable for fiber-suspended droplets. In addition, the experimental conditions were found to be highly repeatable yielding a relative standard deviation in measured quasi-steady evaporation rate of 0.9% for twelve test runs with butanol [36].

3. Results and discussion

In this section, the results obtained from the sequential images of droplet and flame evolution of the heavy oil droplet are discussed. Firstly, the effect of ambient oxygen concentration on the evaporation and burning characteristics are presented in section 3.1. For the sake of simplicity, the experimental results analyzed in section 3.1 are reported considering one representative test from the ensemble of tests conducted for each condition. Since the whole consumption history of the droplet was recorded, the different processes undergone by the droplet during the liquid and solid phases are individually analyzed and discussed in section 3.1.1 and 3.1.2, respectively. Secondly, numerical metrics such as ignition delay time, micro-explosion regimes, cenosphere size and time metrics are calculated for a more quantitative assessment of the previously described processes, being presented in section 3.2. In this case, all the repetitions conducted for each condition are used for evaluation.

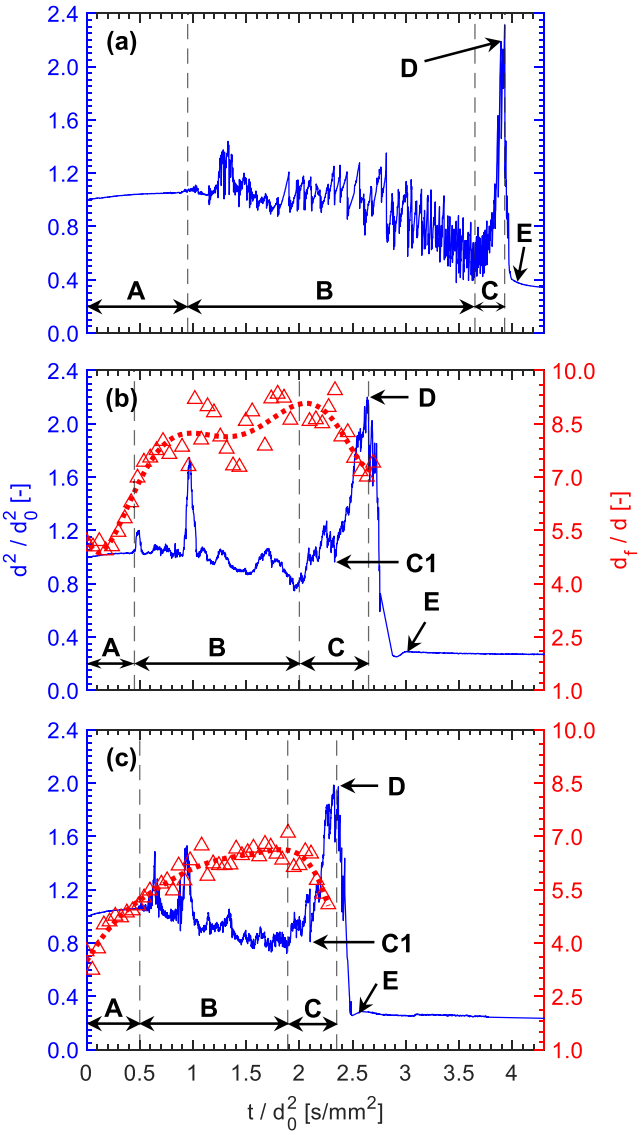

Fig. 3. Temporal evolution of normalized d^2 and flame stand-off ratio measured for heavy oil droplets under different test conditions:(a) 0% O_2, d_0 = 505 μm (b) 5% O_2, d_0 = 501 μm and (c) 10% O_2, d_0 = 527 μm. The instant t = 0 has been defined when T_∞ > 1286 K for case (a) and at ignition for cases (b) and (c).

3.1. Effect of ambient oxygen content on droplet characteristics

3.1.1. Liquid stage

The first stage in the evolution of heavy oil droplets is the evaporation of liquid where the droplet size changes. Accordingly, the droplet size history is obtained in terms of normalized d^2-t curve for all oxygen concentrations and shown in Fig. 3. For 5% and 10% O_2 ambient cases, an envelope flame develops around the droplet. Hence, the flame stand-off ratios are obtained for these cases (Fig. 3(b) and (c)) and plotted alongside. To aid the understanding of Fig. 3, representative images illustrating important events experienced by the droplet and its simultaneous flame (only for combustion case) during its lifetime are extracted and are shown in Fig. 4. In concurrence with previous works [20,23,24], the experimental results clearly show that the liquid stage displays successive distinct stages. They are identified as follows: frozen evaporation (A), disruptive evaporation (B), thermal decomposition and polymerization (C + D) and cenosphere formation (E), as marked in Figs. 3 and 4. While for brevity the subsequent discussion is mainly

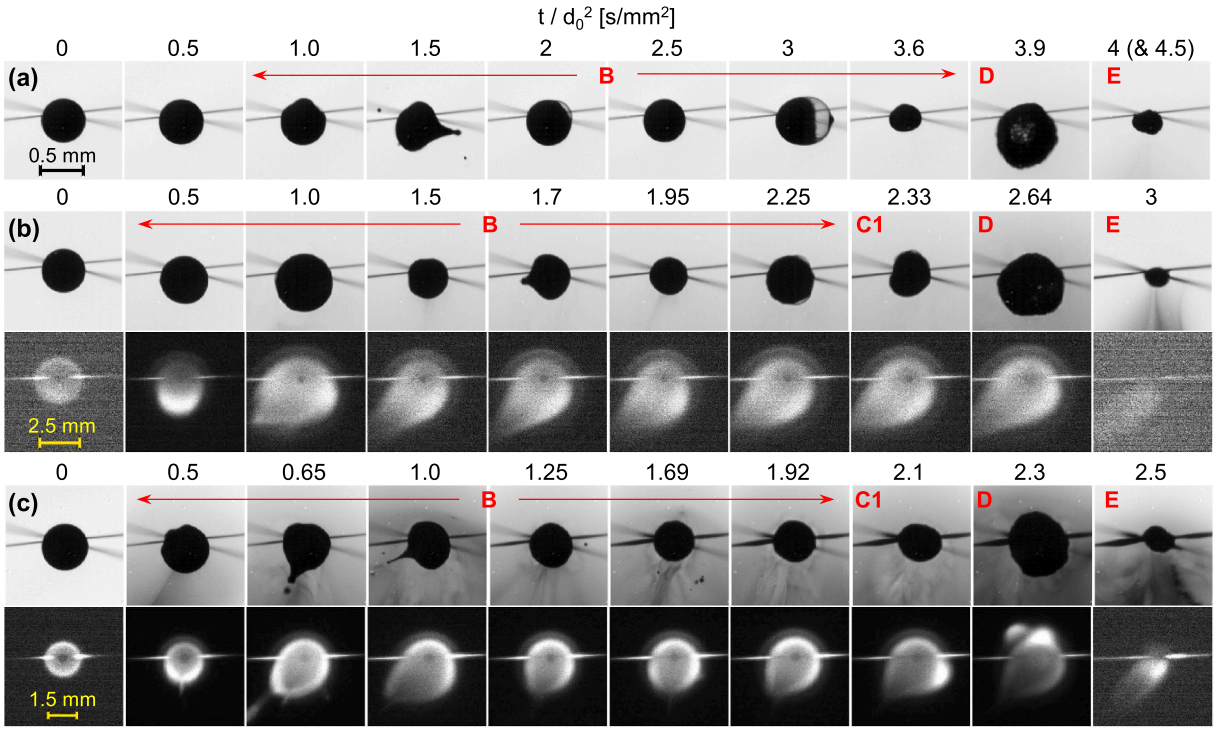

Fig. 4. Evolution of droplet and simultaneous flame shapes of heavy oil droplets for the cases represented in Fig. 3. (a) 0% O_2, $d_o = 505$ μm (b) 5% O_2, $d_o = 501$ μm and (c) 10% O_2, $d_o = 527$ μm.

centered on the effect of ambient oxygen concentration on the identified stages, the reader may refer to the previous works for more details about these stages.

It is evident from these figures that the liquid stage of heavy oil consumption generally comprises two main regions: smooth evaporation (zone A) and fluctuating evaporation (zones B–E). During zone A, the droplet undergoes initial heat up where its surface remains spherical and smooth, without showing any perturbation. The evaporation is limited to the surface and can be termed as 'frozen vaporization' [24,39], most of the heat input to the droplet being used to heat up the liquid, while some preferential evaporation of the lighter compounds is also expected to occur at the surface. However, the dominant effect in this phase is the increase of liquid temperature, as it can be ascertained from the sustained increase in droplet size due to thermal swelling. The droplet remains perfectly spherical during these initial instants, as evident in the images displayed in Fig. 4. With the presence of O_2 in the ambient and since the gas temperature is higher than the auto-ignition temperature of volatile vapors, ignition occurs, leading to an envelope flame around the droplet (see Fig. 4(b) and (c)). The adiabatic flame temperature (T_f) for 5% and 10% O_2 is estimated as 1755 K and 2192 K, respectively, increasing the heating rate and accelerating the initial heat up as compared to the oxygen-free evaporation case (Fig. 3(a)). This is also quantitatively verified later in section 3.2.5. Moreover, the flame stand-off ratio (FSR) progressively increases with time due to the sustained increase in the rate of fuel vapors produced at the droplet surface. This increase is quite smooth and without fluctuations for both cases (Fig. 3(b) and (c)). As expected, with higher O_2 concentration in the ambient, the flame stays closer to the droplet, leading to smaller FSR values and a faster conversion.

Completion of zone A is usually marked by a deformation in the droplet, either accompanied by abrupt micro-explosions or, in some cases, strong puffing events. These puffing/micro-explosions events are described in detail in Ref. [7], and their onset identifies the beginning of disruptive evaporation zone (B), which can be classified in two different types. In the first category, the droplet surface is still in liquid phase and nucleated vapor bubbles at the droplet core are able to move towards the droplet surface and escape. In such cases, the droplet swells locally and ejects puffs of child droplets at high speed. The reactive force from this ejected puff causes the droplet to deform, regaining just after ejection its original spherical shape (see image at $t/d_0^2 = 2.5$ in Fig. 4(a)), proving in this manner the liquid state of the surface. The puffing events in pure evaporation tests (0% O_2) were found to be of this nature with sequential escaping of child droplets that, in addition to inner and surface evaporation, led the parent droplet to regress up to $d^2/d_0^2 \sim 0.4$ by the end of zone B. On the contrary, in both cases of combusting droplets (Fig. 4(b) and (c)), such events in zone B were characterized by multiple puffing sites (see image at $t/d_0^2 = 2.25$ in Fig. 4(b)), causing faster ejection of child droplets while the droplet appeared frothed [24,40]. This frothing slightly perturbs the flame, as it can be assessed by the higher scattering in FSR values in zone B (as compared to zone A) in Fig. 3. These perturbations are more marked for the 5% O_2 case, since flames are weaker and further away from the source of fuel vapor. On the contrary, the steeper fuel compositional gradients for the 10% O_2 condition eases the return of the flame front to the stoichiometric location after a disruptive event. It is also worth to note the gradual increase in flame stand-off ratio during zone B in Figs. 3 and 4 ((b) and (c)), ascribed to the fuel accumulation effect [41]. Additionally, due to steeper temperature gradients and stronger thermophoresis forces acting on soot particles for the 10% O_2 condition, a larger amount of soot is confined inside the envelope flames for this case. For both combusting cases, the droplet regressed up to $d^2/d_0^2 \sim 0.8$ in this manner, ending this zone B at a droplet diameter squared that doubles that of the pure evaporation case (i.e., a droplet size ~1.41 times larger than the former).

As proposed in previous works [24,39], the onset of thermal decomposition (zone C) is marked by a local minimum in the droplet size history. At this point, the droplet is sufficiently depleted of volatile compounds and its temperature is sufficiently high that the predominant heavy fractions of HFO start to thermally decompose through pyrolysis reactions. These reactions were reported in Refs. [18,24] to occur (for similar heavy oils) at liquid temperatures above ~700 K. Although the

measurement of droplet temperature was avoided in this work due to the potentially significant deviations that might be introduced by thermocouples [36], the transition between phases can be ascertained from the droplet size evolution curves, as well as from the images displayed in Fig. 4. Most notably, the surface of the droplet is no longer smooth after transitioning to zone C, pointing to an increased viscosity of the droplet surface shell. The gases generated in pyrolysis reactions cause the droplet size to increase steeply but also to contract suddenly as they escape. It must be noted that, at this point, the droplet only contains heavy compounds. Hence, in contrast to the volatiles escaping in zone B, gases find a greater resistance to escape the droplet, as the heavy compounds at the droplet surface start to layer up causing the development of a viscous outer shell [16]. Pyrolysis is a highly endothermic process and hence, at the end of this stage, the droplet liquid temperature would be expected to fall, causing the end of process at point C1. However, if the heat transfer from the ambient is high enough, the remaining heavy compounds will start to polymerize as soon as the liquid temperature reaches T ~840 K [24]. Polymerization is a highly exothermic process, and hence, its heat release contributes to drive pyrolysis. This combination of pyrolysis and polymerization constitutes zone C. As the heavier compounds polymerize, the viscous outer shell starts to thicken while the gas generation due to pyrolysis continues, causing the impermeable shell to swell to its peaks value at point D. The shell eventually breaks, allowing the pyrolysis gases to escape, and the polymerized compounds condense into a solid residue as indicated by point E.

As it can be noticed in Fig. 3, the onset of pyrolysis (zone C) occurs much earlier for combustion (5%, 10% O_2) when compared to the pure evaporation case (0% O_2). Therefore, for the case of pure evaporation, events C-E do not occur until all the volatiles have been lost ($d^2/\ d_0^2$ ~0.4). Thus, when the evaporating droplet reaches the pyrolysis temperature (~700 K [24]), the transition from pyrolysis to polymerization stage is quite rapid. Compared to 0% O_2, in the cases with combustion, zone C starts earlier (d^2/d_0^2 ~0.8) and continues for a longer period since the heat transfer rate due to the envelope flame (radiation and gas conduction from a higher T_f) is higher and HFO is known to easily absorb radiative heat which is directed towards its core [12]. Hence, unlike the oxygen-free conditions, when pyrolysis starts, few volatiles may still be present within the droplet. Moreover, the polymerization period is also longer for cases (b) and (c), as evident from the width of the peak at location D. This indicates that the polymerized droplet shell is more viscous and impermeable as compared to that formed during pure evaporation. This allows the shell to retain multiple swellings while the pyrolysis gases are trying to escape. Due to the increase in droplet size, a rapid decrease in the flame stand-off ratio is observed in zone C. However, it should be noted that the flame in this zone would mostly correspond to the combustion of pyrolyzed gases escaping the shell, while the measured droplet size corresponds to the porous shell (rather than to a liquid droplet). Therefore, although plotted, from the authors' perspective it may not be correct to consider it as an envelope flame, in the sense of those usually found around evaporating droplets and sustained by the diffusion of the gas vaporized at the droplet surface in conventional liquid droplet evaporation/combustion processes.

Finally, the formation of solid residue occurs, marking the end of liquid stage. This is indicated as point E in Figs. 3 and 4. Depending on the ambient conditions, this cenosphere will be consumed, as it is discussed next.

3.1.2. Solid stage

Cenosphere combustion has been addressed in a number of experimental studies, providing quantitative and qualitative results in terms of different time scales, partial size history, types of events, size ratios or the minimum ignition temperature [20,22,23] while few theoretical models have been presented in Ref. [40]. These works discuss the global data in detail and provide general insights on the burning regimes of cenospheres in hot air (21% O_2). In this work, for the first time, the

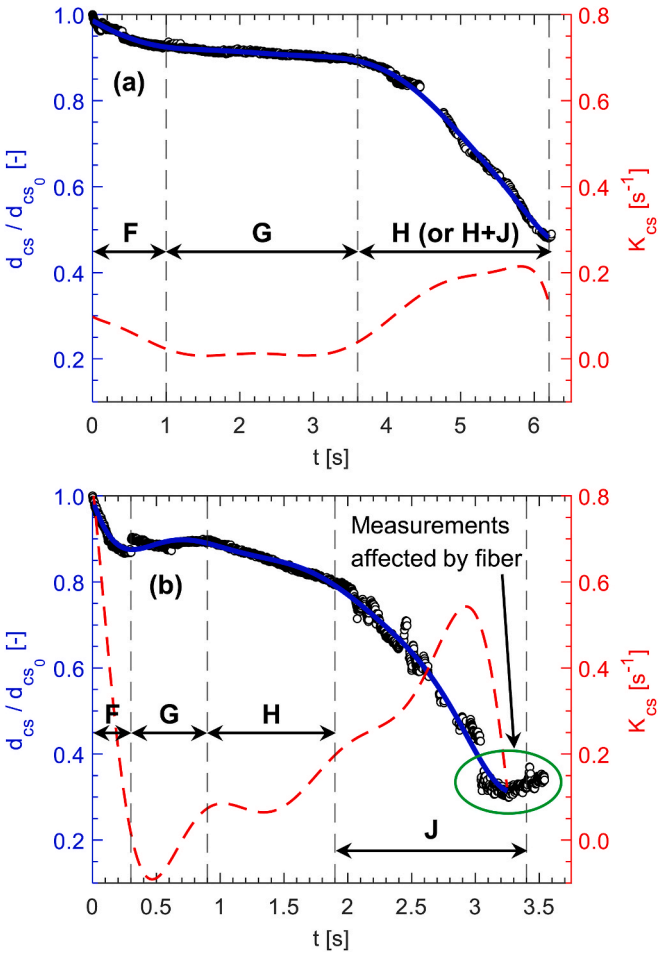

Fig. 5. Normalized burning size history of cenosphere for different test conditions: (a) 5% O_2, d_0 = 490 μm, d_{cs0} = 212 μm and (b) 10% O_2, d_0 = 456 μm, d_{cs0} = 212 μm with their burning regimes identified. t = 0 marks the instant of cenosphere formation.

different cenosphere burning regimes are experimentally identified and discussed along with its size and shape history for different (and realistic) oxygen conditions. Despite the presence of significant water vapor in the hot co-flow, in absence of oxygen (0% O_2 condition), the cenosphere is noted to retain its mass and size (at least for residence times in the order of a few seconds explored in this work). Therefore, in this section, only the cases with ambient oxygen concentrations of 5% and 10% are considered. The point at which the cenosphere is formed in Fig. 3 (i.e. at point E) is assigned as t = 0, and the size of the cenosphere at that initial instant (d_{cs_0}) is noted. Using these new references, the normalized size evolution of the burning cenosphere is obtained and shown in Fig. 5, being the sequential images of the consuming cenosphere shown in Fig. 6. In addition, a closer look on the data so obtained reveals that: (1) the cenospheres generated from combusting droplets at 5% and 10% O_2 have similar sizes (see Figs. 3 and 4) and structures as per [15,16,26] and (2) the ambient temperature is essentially the same for both cases. Thus, alternatively, it can be said that the data presented in Fig. 5 is equivalent to a test where an isolated cenosphere suspended on a fiber is burning at two different ambient O_2 levels.

The cenosphere oxidation commences immediately after it is formed, since the ambient temperature (1408 ± 20 K during the whole oxidation process) is much higher than the reported minimum ignition temperature of 1150 K [25]. Some amount of soot generated due to the envelope flame (visible in Fig. 4) accumulates on the fiber as well as it deposits inside the blowholes and pits of the cenosphere [11]. For 10% O_2 ambient, soot accumulation is much more pronounced than for the 5%

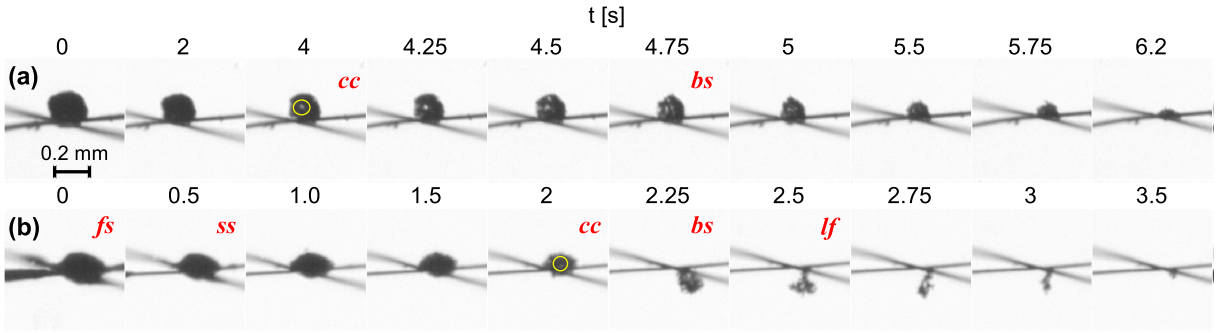

Fig. 6. Evolution of cenosphere shape for cases represented in Fig. 5. (a) 5% O_2, d_0 = 490 μm, d_{cs0} = 212 μm and (b) 10% O_2, d_0 = 456 μm, d_{cs0} = 212 μm. Representative instances of fiber soot (*fs*), surface soot (*ss*), central cavity (*cc*), basket or skeleton structure (*bs*) and lacy fragments structure (*lf*) are marked.

O_2 case. Therefore, the first stage of cenosphere burning is soot burnout, represented as zone F in Fig. 5. During this period, the soot burning leads to an apparent decrease in cenosphere size, or rather it is more appropriate to say that this reveals the actual surface and size of the cenosphere. Despite the greater soot accumulation for the 10% O_2, the higher oxygen concentration causes a faster soot burnout, zone F is almost four times shorter that at 5% O_2. Similar soot burnout has also been reported in Ref. [25] which in the present configuration is clearly visible.

After this, the second stage (zone G) begins, where there is hardly any change in the cenosphere size. This zone is especially relevant for the 5% O_2 case, as evident from Figs. 5(a) and 6(a). The fact that the particle size remains constant suggests that the combustion process is kinetically controlled, and oxidation occurs both at the internal and external surfaces because oxygen diffusion through the pores is faster than the reaction rate. Hence, solid consumption occurs over the whole volume of the cenosphere, with a larger contribution of internal parts due to their much greater area compared to the outer surface. Thus, this zone G can be considered as equivalent to the commonly referred 'regime I', corresponding to constant-size combustion of oil-coke (or porous char) particles [40].

To describe in more detail this stage and the trend of cenosphere consumption, a 10th order polynomial is fitted to the experimental d_{cs}/d_{cs_0} data and is shown as a continuous blue line in Fig. 5. The rate of change of normalized cenosphere diameter (K_{cs}) is obtained by applying eq. (1) on this polynomial fit and is plotted as a dashed red line in the same figure.

$$K_{cs} = \frac{d\left(d_{cs}/d_{cs_0}\right)}{dt} \tag{1}$$

For the case of 5% O_2, K_{cs} is practically zero in zone G, thus indicating that the solid residue is not changing its size, and its consumption must be dominated by reactions inside the cenosphere. This is readily confirmed by the smooth external surface of the cenosphere in Fig. 6(a). For the case of 10% O_2, the interval of constant particle size (zone G) is much shorter, and during most of the oxidation process the size gradually decreases (zones H and J). This difference among tests with 5% and 10% O_2 is consistent with a faster reaction kinetics for the later, so that, the heterogeneous oxidation seems to reach a mixed regime: 'regime II + III' [40], controlled by both diffusion and kinetic rates. In that case, even though the internal surface area is much larger than the outer one, the oxygen is partially consumed before reaching the inner surfaces, reducing the oxidation rate per unit of area. As a result, in the mixed heterogeneous regime, particle size decreases, as it is in fact observed for zone H in Fig. 5 and becomes clearly more relevant for the case with higher oxygen availability (Fig. 5(b)). Interestingly, this transition from zone G to H is clearly visible in Fig. 6(b), where the cenosphere surface appears smooth in zone G but more irregular (pits due to oxidative attack) in zone H. The lower oxygen concentration extends zone G by ~6 times at 5% O_2 with respect to the case with 10% O_2. Another important feature during this period is that a central cavity in the core of the cenosphere becomes visible at the end of zone G for 5% O_2, whereas this is delayed until the end of zone H for 10% O_2. This is fully consistent with the interpretation postulated above that for 10% O_2, the majority of cenosphere combustion occurs in a mixed regime, with reduced oxygen availability, and hence lower specific oxidation rate, at the inner surfaces.

After the cavity becomes visible, the cenosphere size decreases sharply in both cases and it transforms into a skeleton or basket-type structure, with very thin walls that are rapidly consumed and destroyed resulting in a faster size reduction (zone J). The time scale of zone J is of the order of the preceding stages (F-H) for both cases, implying that zone J is the limiting step for achieving complete combustion of cenosphere. Different behaviors for 5% and 10% O_2 cases are seen. For the 5% O_2 test, although the skeleton is visible, due to relatively low oxygen availability, the consumption rate is slower and appears to be limited by surface reactions. After some time, the skeleton collapses and burns even more slowly. In some other cases at 5% O_2, the skeleton fragmented after zone G. Hence, this zone has been marked as H or H + J in the case of 5% O_2. For the case of 10% O_2, the skeleton always disintegrated into lacy fragments. Besides, during the last stages of cenosphere evolution, the measurements were affected by the inclusion of some portion of the fiber. Therefore, the normalized cenosphere size does not fall to zero in Fig. 5.

Thus, based on the above discussion and the stages observed in Refs. [25,40], the following successive stages for cenosphere combustion are identified: surface soot burn-off (F), constant diameter burning (G), mixed regime burning (H) and skeleton + fragmented burning (J).

3.2. Quantitative analysis of the effect of ambient oxygen on droplet evolution

In this section, the experimental observations obtained from tests at

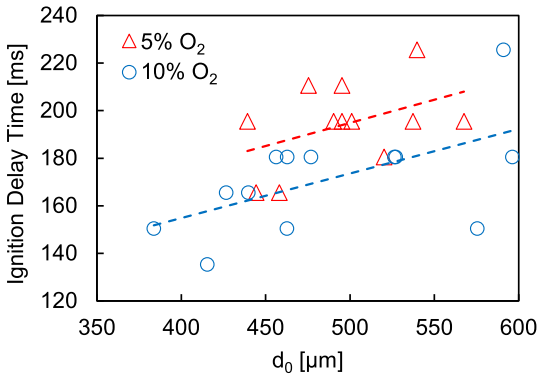

Fig. 7. Ignition delay time vs d_0 for 5 and 10% O_2 in the co-flow.

different oxygen concentrations are further quantified in terms of metrics defined to parameterize the different aspects. In all cases, the reported data corresponds to the whole ensemble of tests conducted for each condition.

3.2.1. Ignition delay time

The ambient conditions (1336 ± 50 K) in the present work are well beyond the reported auto-ignition temperature of heavy oil (680 K [42]). Hence, for the cases with co-flow containing 5% and 10% O_2, an envelope diffusion flame is spontaneously formed around the droplet. The ignition delay time can be obtained from these tests, as the interval between the instant at which the droplet is exposed to hot gases (i.e. when the air shield is closed, as explained in section 2.2), and the first appearance of an envelope flame in the flame images. This metric is plotted in Fig. 7 for the two oxygen conditions and different droplet sizes, covering the d_0 range of 380–600 μm.

For the same droplet size, longer ignition times are observed for the lower oxygen condition. This result seems logical, since ambient temperature is essentially the same for both oxygen conditions and the ignition delay time will depend on the mixing time required by the fuel vapor and oxidizer to attain flammable conditions, which can be of the order of the lower flammability limit. Oxygen availability also governs the distance between the flame front and the droplet, as seen from the FSR in Fig. 3(b) and (c). For a given oxygen concentration, the ignition delay increases for larger droplets, as also observed in Refs. [15,22], which is attributed to their greater thermal inertia. It should be noted that some datapoints in Fig. 7 deviate from the general trendline, due to the relatively low frame rate (one frame every 15 ms) used in the flame imaging optical setup, resulting in a non-negligible random uncertainty. Overall, the average ignition delay times obtained for 5% and 10% O_2 test conditions are 194 ± 17 ms and 171 ± 22 ms, respectively, where the uncertainty interval represents the standard deviation in the data group.

3.2.2. Micro-explosion regimes

The normalized droplet evaporation curves obtained for pure evaporation show several differences with respect to those with combustion. The droplet undergoes events such as puffing and micro-explosion, which are a consequence of volatilized components escaping through the thickening oil membrane at the droplet surface. As proposed in Ref. [43], the occurrence and classification of these events can be quantified using the *expansion ratio* (ER), as defined in eq. (2), being d_p and d_v the droplet size peak and valley values during the onset of a fluctuating evaporation event (i.e., frame just before and after the event). The expansion ratio is calculated from the curves recorded during the liquid disruptive evaporation stage of all tests (zone B in Fig. 3) and the different regimes are classified according to: $1.05 \leq ER \leq 1.2$ as puffing regime, $1.2 < ER < 2$ as weak micro-explosions and $ER \geq 2$ as strong micro-explosions [43]. Following this classification, the number of events detected in the different tests are shown in Fig. 8.

$$ER = d_p^2/d_v^2 \tag{2}$$

In these tests, no strong micro-explosions are observed for either evaporating or combusting droplets of heavy oil which, instead, are typically found for emulsified droplets [29,44]. The results in Fig. 8 as well as the normalized size history in Fig. 3 clearly show that puffing and weak micro-explosion events dominate the droplet evaporation. These events initiate with a frequency (number of events per second) as low as 50 Hz and exponentially increase up to 800 Hz, which has also been reported in Ref. [20] as up to 1 kHz. For the combustion cases (5% and 10% O_2), the number of puffing events obtained with this metric is less than for pure evaporation, despite the heat transfer due to envelope flame is higher. This is because the disruptive evaporation of a combusting droplet is observed to undergo multiple nucleation and escape sites in contrast to the sequential puffing events observed in the pure

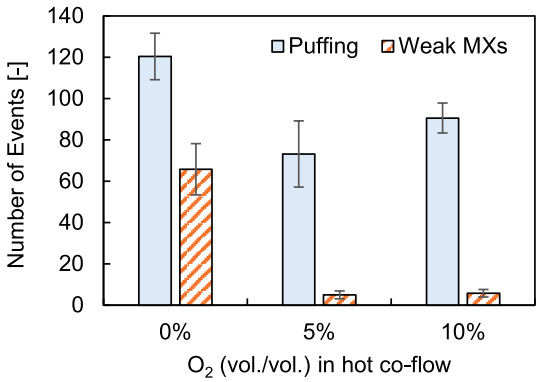

Fig. 8. Effect of $\%O_2$ on the number of droplet expansion events, classified as 'puffing' and 'weak micro-explosions (MXs)'. The group average value is plotted with uncertainty bars showing the standard deviation of the group.

evaporation case. Thus, although there is an increase in the number of very weak puffing events, they do not actually qualify for their inclusion in Fig. 8 since their $ER < 1.05$. Besides, the number of micro-explosions obtained (also observed in Fig. 3) is also significantly less for a combusting droplet as compared to pure evaporation case. This could be attributed to the faster release of the vapors generated, reducing the probability of forming large bubbles and building significant pressure inside the droplet that might result in droplet shattering.

3.2.3. Shell swelling ratio

The viscous droplet shell inflates to its peak value (marked as point D in Fig. 3) when the pyrolysis gases generated in zone C cannot escape. The ratio of this peak shell (droplet) diameter to that of the initial droplet size is calculated as given in eq. (3) to obtain the *shell swelling ratio* [20,45] and plotted in Fig. 9 for all the tests. The results depict a decreasing trend with oxygen concentration. This can be ascribed to the fact that, as ambient O_2 increases, the relative duration of zones C + D also tends to grow, with a clear increase in the duration of zone C between evaporation and combustion cases (Fig. 3). In addition, due to a higher heating rate for combustion conditions, a greater amount of pyrolysis gases are generated and violently escape [45,46], which creates local ejection sites. On the other hand, the shell swelling ratio for pure evaporation is higher than in combustion conditions. This is because when pyrolysis starts, all the volatiles have been lost and hence, the droplet shell must be more viscous and impermeable which offers a higher resistance for the gases, thereby causing an abrupt expansion of the droplet shell.

$$\text{Shell Swelling Ratio} = \sqrt{d_{max}^2/d_0^2} \tag{3}$$

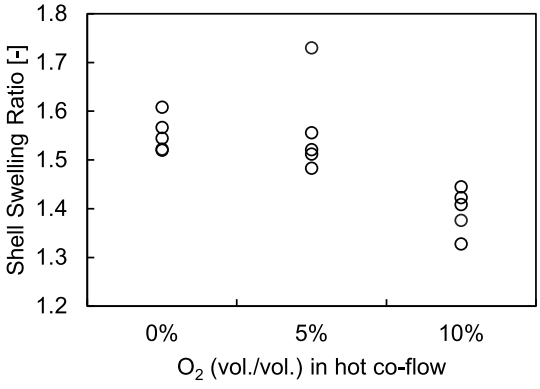

Fig. 9. Effect of $\%O_2$ in the co-flow on peak swelling ratio of the droplet.

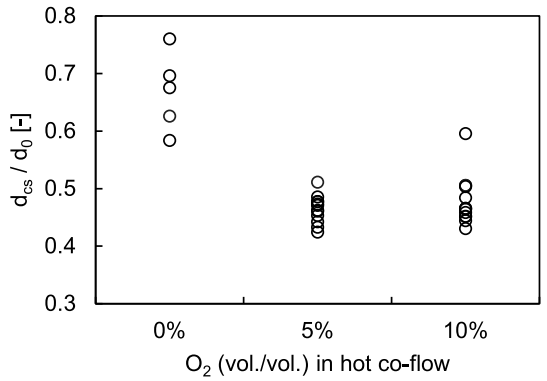

Fig. 10. Effect of %O_2 in the co-flow on the normalized cenosphere size.

3.2.4. Cenosphere size

As discussed before, the cenosphere is formed at the end of liquid stage consumption in each test (marked as point E in Fig. 3). The projected area measured in the image is used to obtain its equivalent sphere diameter, d_{cs}. This cenosphere diameter is normalized by the initial droplet size (d_{cs}/d_0) and plotted in Fig. 10 for different ambient O_2. The mean normalized size ratio of the cenospheres formed when subjected to high temperature ambient containing 0%, 5% and 10% O_2 are obtained as 0.66 ± 0.06, 0.46 ± 0.02 and 0.47 ± 0.04, respectively. The cenospheres produced from combusting droplets are quite similar in size at 5% and 10% O_2, whereas those produced from pure evaporation are ~40% larger. This clearly shows that results based on combusting droplet tests may significantly lead to underestimate the size of cenosphere formed under reducing conditions, which is specifically important for gasification applications. The difference in cenosphere size can be related to their morphological evolution, as reported in Refs. [14–16,25]. It is worth to note that, in all cases, the cenosphere size obtained is smaller than the initial droplet diameter since the asphaltene content is relatively low (see Table 2) and, due to the high temperatures explored, the droplet undergoes strong disruptive evaporation that causes early local ejection of vapors before a thick shell is able to form. This is consistent with the observations in several previous works [9,13,25,47,48].

The existence of a correlation between cenosphere size and n-heptane (n-C7) asphaltene content in the fuel has been well established and is a topic addressed in almost all works cited herein (see e.g. Refs. [9,14,15,20,45,48]). Therefore, the cenosphere size obtained in the present work is also plotted against n-heptane asphaltene and compared with previously reported values in Fig. 11. Wherever necessary (including the data from the current work), an approximate value of n-heptane asphaltene is obtained from n-pentane (n-C5) asphaltene data by considering the ratio of heptane-to-pentane asphaltene as 0.8 [49,50]. As found in several published works, the normalized cenosphere size increases linearly with the asphaltene content when this content lies below 8% wt [15,26,45]. Interestingly, although most of the studies have been carried out in hot fresh air (i.e. 21% O_2), the measurements from the present work for combusting droplets at 5% and 10% O_2 also follow the same trend, whereas the measurements for the pure evaporation case (0% O_2) yield larger cenospheres, clearly away from the general trendline. This implies that cenosphere size varies depending if there is oxygen available or not, but largely unaffected when combusting under different ambient O_2, which is consistent with cenosphere formation pathways proposed by Refs. [16,26]. As a word of caution in interpreting Fig. 11, the authors' note that in many cases particulate samples are collected at the exhaust, particularly for tests with free droplets and spray combustion which allows them to undergo partial oxidation after their formation. In such cases, these measurements are expected to result in some reduction in size compared with freshly formed cenospheres. Instead, in the present case, the measurement is referenced at the exact instant of cenosphere formation (point E in Fig. 3).

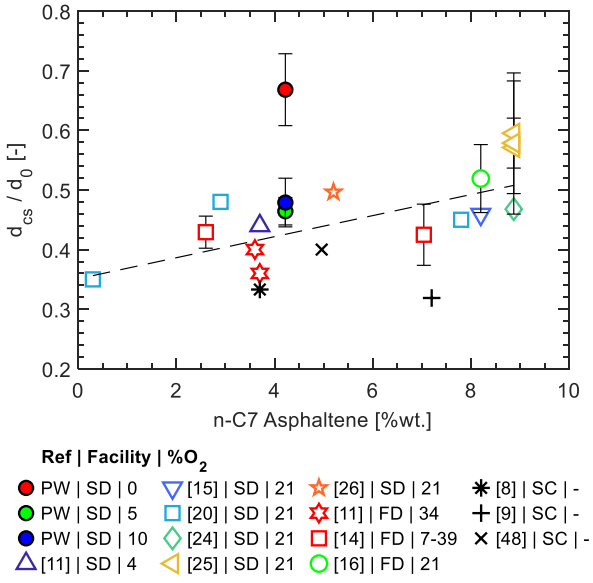

Fig. 11. Comparison of cenosphere size in the present work (PW) with respect to those reported in literature for different asphaltene contents. The type of facility used: suspended droplets (SD), free droplets (FD), spray combustion (SC) and the %O_2 in the ambient test conditions are marked in the legend. The uncertainty bars represent the standard deviation in the group tests.

3.2.5. Time metrics

The discussion in section 3.1.1 regarding the evolution in the liquid stage establishes two main periods: initial heat-up with smooth evaporation (zone A) and fluctuating evaporation (zone B + C). Time metrics for both periods have been extracted from the normalized droplet size histories and presented in Fig. 12. The *initial heat-up time* (t_i) is defined as the time elapsed between the test start and the onset of the first puffing event. The *total evaporation time* (t_l) refers to the time elapsed between the test start and the instant when the cenosphere is formed, marking the end of liquid evaporation (point E in Fig. 3). The difference between the initial heat-up time and the total evaporation time is defined as the *fluctuating evaporation time* ($t_{fl} = t_l - t_i$). The normalized total evaporation time monotonically decreases as the oxygen level in the gas increases from 0 to 10%. Similarly, the initial heat-up time is also reduced due to the increased temperature above T_∞ at the envelope flame, enhancing heat transfer to the droplet.

Additional tests were also conducted in this study to characterize the

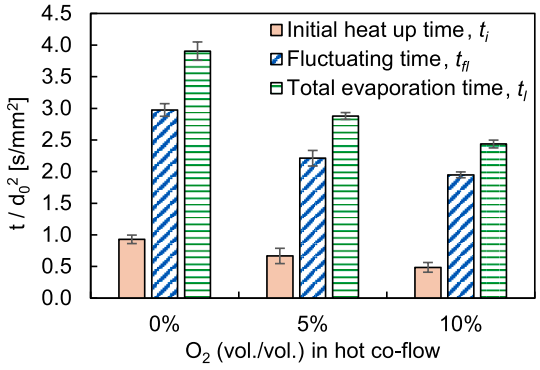

Fig. 12. Time metrics of liquid fuel consumption regimes for heavy oil droplet. The group average value is plotted with uncertainty bars showing the standard deviation of the group.

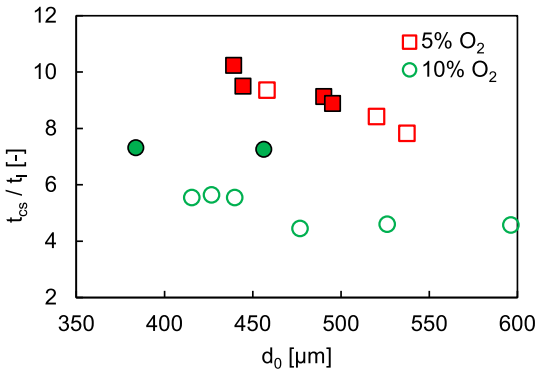

Fig. 13. Effect of %O_2 in the co-flow on solid-to-liquid consumption times with different initial droplet sizes. Solid markers identify cases in which complete burnout of cenosphere was observed.

cenosphere burning regimes and obtain the total cenosphere consumption time. The data so obtained are presented in Fig. 13 as the ratio of solid-to-liquid consumption times, where the liquid consumption time is represented by the *total evaporation time*, t_l, and the *solid consumption time*, t_{cs} is evaluated as the time from cenosphere formation to its full consumption. As discussed in section 3.1.2, during the last stages of cenosphere burning, the skeleton and fragmented cenospheres are extremely fragile and light in weight, and in many cases, fell off the suspension fibers. Similar difficulties in experiments with cenosphere burning have also been reported in Refs. [22,25]. Nevertheless, the visual records of such videos show that the major portion of cenosphere was burnt, and hence it is reasonable to consider these events also as indicative of the time to complete cenosphere burning. In any case, the data in Fig. 13 are identified by two different markers: solid symbols when the complete history was recorded whereas hollow markers indicate that the cenosphere skeleton dropped at the end. The difference in terms of t_{cs}/t_l between both kind of tests is estimated to be about 9.5 and 30.5% for the 5 and 10% O_2 condition, respectively. As it is evident, the most reliable data in Fig. 13 corresponds to cases where the full cenosphere history could be recorded. Regardless of these differences, Fig. 13 clearly shows that the solid consumption time for 5% O_2 is significantly longer, about twice, than for 10% O_2. This could be attributed to the longer zone G observed in 5% O_2 whereas the time scale for zone H + J is of the same order in both cases. For the present work, the solid-to-liquid consumption time ratio obtained for 5% and 10% O_2 is of the order of 9–11 and 5–7, respectively which is quite high in comparison to those reported in Ref. [23] as 1.3–2 for 21% O_2 at 1200 K. All these results consistently confirm, as it could be expected, a strong dependency of cenosphere consumption time with oxygen concentration. Since the oxidation of these carbonaceous particles is normally the limiting step to achieve complete fuel conversion and low particulate emissions in practical applications, due attention needs to be paid to characterize this process, which also requires a careful selection of reference conditions.

The droplet consumption times obtained from the experimental tests can also be used to obtain global regression rate coefficients (or burning rate) for heavy oil droplets [9,17,20]. Two different rate coefficients are calculated based on *consumption time of liquid*, K_l, and *liquid + solid*, K_t, as defined in eqs. (4) and (5), respectively. Average values for the whole group are provided in Table 3, where the standard deviation is also shown to indicate the statistical scatter in the group. As expected, these global burning rates increase monotonically with %O_2 in the co-flow due to higher heating rates as more oxygen is available. It is interesting to note that, in the existing literature, the values reported for K_l and K_t with 21% O_2 ambient are found to be in the range of 0.5–1.5 mm^2/s [9,17,19,20,23] and 0.2–0.4 mm^2/s [20,23], respectively. These are significantly higher than those obtained in the present work, thereby showcasing the impact of ambient conditions.

Table 3
Global regression rates based on global time scales. The uncertainty represents the standard deviation in the group data obtained in the current work (0, 5 and 10% O_2).

Atmosphere	K_l [mm^2/s]	K_t [mm^2/s]
0% O_2	0.1404 ± 0.0164	–
5% O_2	0.2667 ± 0.0082	0.0348 ± 0.0027
10% O_2	0.3141 ± 0.0171	0.0646 ± 0.0110
21% O_2	0.5–1.5 [9,17,19,20,23]	0.2–0.4 [20,23]

$$K_l = \frac{1 - d_{cs}^2/d_0^2}{t_l}\ mm^2 \Big/ s \tag{4}$$

$$K_t = \frac{1}{t_l + t_{cs}}\ mm^2 \Big/ s \tag{5}$$

The values given in Table 3 complement the available data, providing a complete picture for different ambient O_2 that a droplet may encounter inside a real flame and can be conveniently utilized for numerical simulations or empirical calculations. It should be noted that, in real combustion equipment, cenosphere burning occurs partly in the flame and partly in the post-flame region, where oxygen concentration is well below that of fresh air and gradually approaches the excess oxygen in flue gases. Therefore, the values reported in this work for intermediate-to-low oxygen concentrations are thought to provide reference values representative of actual cenosphere consumption rates in practical applications.

4. Conclusions

In the present work, experimental studies with isolated droplets of heavy oil ($d_0 \sim 500$ μm) are conducted in different realistic, flame-like atmospheres. High temperature conditions of 1336 ± 50 K with 0, 5 and 10% O_2 concentration in the co-flow have been explored. Infrequent in the literature, these conditions aim to represent the ambient actually seen by droplets in real applications, being therefore not only relevant for combustion but, partially, also for heavy oil gasification. The full temporal evolution of droplet size, cenosphere size and envelope flame have been studied in a suspended-droplet setup designed to minimize the impact of experimental artifacts. Novel results of practical relevance have been obtained on a number of aspects not or scarcely covered in the available literature on the thermal conversion of heavy oil droplets. On the one hand, whereas practically all available results have been obtained at 21% O_2, experimentation at low and variable oxygen concentrations is clearly needed to correctly describe the droplet behavior in practical applications. On the other hand, cenosphere burning being the limiting step in heavy oil conversion, the evolution of cenosphere size has been specifically studied for different (low to intermediate) oxygen concentrations. Finally, detailed experimental characterization of the liquid stage has been achieved, also including the use of CH* chemiluminescence to detect the location of the true envelope flame, as a key parameter for the characterization of droplet combustion (to the authors' knowledge, not previously reported for heavy oil).

Besides a thorough qualitative description of the different stages undergone by the droplet, an effort has been made to extract a range of selected metrics suitable to quantitatively analyze the different phenomena observed as well as to evaluate the specific influence of oxygen concentration. These are some of the main conclusions and new findings obtained in this work.

1. Marked differences have been found between the evolution of heavy oil droplets depending on oxygen concentration. In pure evaporation (0% O_2) ambient, the disruptive evaporation behavior of the droplet consists of sequential puffing events with weak micro-explosions, whereas for combusting ambient (5%, 10% O_2) multiple nucleation

(and puffing) sites are observed with a significantly lower number of weak micro-explosions.
2. Additionally, the pyrolysis and polymerization stage in oxygen-free ambient begins only when the droplet is devoid of most of the volatiles ($d^2/d_0^2 \sim 0.4$) which is in sharp contrast to that observed in combusting droplet cases, where it begins quite earlier ($d^2/d_0^2 \sim 0.8$). This results in a longer pyrolysis zone and a decrease in peak droplet swelling as the ambient O_2 increases. This decrease in the final swelling of the droplet points to a more viscous and impermeable shell for the oxygen-free ambient.
3. The cenospheres formed from droplet combustion at 5% and 10% O_2 are quite similar in size ($d_{cs}/d_0 \sim 0.46 - 0.47$) whereas those generated under pure evaporation conditions are ~40% larger than the former ($d_{cs}/d_0 \sim 0.66$). Therefore, bigger cenospheres are expected to be formed in very low oxygen conditions (e.g. flame core) or for heavy oil gasification applications as compared to the values normally obtained for combustion in fresh air.
4. Special attention has been devoted to characterize cenosphere burning, which in many cases is the most critical, limiting factor in the design of clean and efficient HFO combustion equipment. For the first time, the temporal evolution of the cenosphere size has been obtained and the distinct stages have been identified for a high-temperature ambient with 5% and 10% O_2. The results show that, as ambient oxygen content increases, the dominant burning stage shifts from constant size burning to a mixed regime. Nevertheless, the last solid combustion stage (skeleton + fragmented burning) shows a similar time scale as the preceding stages, irrespective of the ambient oxygen availability, which implies it to be a controlling step in cenosphere combustion.
5. The solid-to-liquid consumption time ratio extracted for 5% O_2 is found to be significantly larger, about twice, than that obtained for the 10% O_2 case, with values lying in the range of 9–11 and 5–7, respectively. These values significantly differ from the commonly used and reported value of ~2 for 21% O_2, clearly stressing the challenges posed by the slow conversion of the solid cenospheres, particularly for oxygen deficient conditions (such as those found in the downstream zone of furnaces/gasifiers).
6. The diameter of the actual envelope flame as detected from CH* chemiluminescence has been characterized for the first time for HFO droplets. The flame stand-off ratios obtained show that as ambient O_2 doubles, the flame stays ~1.25 times closer to the droplet, thereby increasing the liquid droplet regression rate by ~1.17 times. Whereas in absence of flame, the liquid droplet regresses at a rate which is ~50% slower than the other two cases.

Overall, the experimental results and quantitative analysis reported here compose a notable comprehensive dataset and are expected to constitute a reference study that complements the existing knowledge (mostly based on tests at 21% O_2) with novel results of practical relevance on the evolution of heavy oil droplets.

When it comes to the limitations of the current work, the main one is the fact that both liquid and solid evolutions are obtained by shadowgraphy, based on the projected area of the droplet and cenosphere, respectively. The presence of bubbles inside droplets (due to internal boiling) and relevant void fractions inside cenospheres increases the uncertainty of the experimental data and related discussion, since the size reduction rate is not exclusively caused by the consumption of the liquid/solid mass. The measurement of the evolution of the droplet/cenosphere mass would be a most notable addition, although, to the authors' knowledge, no experimental setup has been able yet to obtain these data for single droplets under sufficiently realistic conditions. The measurement of the liquid and solid temperatures by means of non-intrusive methods would also be a notable addition, without any known precedent for HFO droplets. Another limitation of the current study is the fact that all tests were performed under atmospheric pressure, while some relevant applications (e.g., gasifiers) usually operate at higher pressures. Assessing the impact of pressure on the obtained results would be a relevant addition to the state of the art, as it would be the measurement of species generated around the droplet for the different stages of liquid and solid conversion.

Nomenclature

$\%O_2$	Oxygen concentration in the free stream dry basis, % by vol.
CN	Convection number, -
d	Diameter/droplet diameter, μm or mm
FN	Fiber number, -
FSR	Flame stand-off ratio, -
k	Thermal conductivity, W/(m·K)
K	Regression rate, mm^2/s
Q	Heat transfer to the droplet, kW/m^2
OD	Optical density, -
RN	Radiation number, -
T	Temperature, K
t	Time, s
vol.	Volume, -
V	Velocity, m/s
Subscripts	
0	Initial
∞	Free stream (or ambient)
cs	Cenosphere (solid component of heavy oil)
f	Flame
fiber	Fiber
fl	Fluctuating
g	Gas
l	Liquid
p	Peak
r	Radiation
t	Total
v	Valley

CRediT authorship contribution statement

Taha Poonawala: Writing – review & editing, Writing – original draft, Methodology, Investigation, Formal analysis, Data curation, Conceptualization. **Alvaro Muelas:** Writing – review & editing, Writing – original draft, Supervision, Methodology, Formal analysis, Data curation, Conceptualization. **Javier Ballester:** Writing – review & editing, Writing – original draft, Supervision, Methodology, Funding acquisition, Formal analysis, Conceptualization.

Declaration of competing interest

The authors declare that they have no known competing financial interests or personal relationships that could have appeared to influence the work reported in this paper.

Acknowledgments

This work was supported by the Spanish Ministry of Science and Innovation (MCIN), Agencia Estatal de Investigación (AEI) and "ESF Investing in your future" [project no.: PID2019-109747RB-I00 funded by MCIN/AEI/10.13039/501100011033] along with pre-doctoral fellowship to T.P. [grant number PRE2020-094620]. The authors acknowledge Instituto de Carboquímica (ICB-CSIC) for kindly providing the physicochemical properties of heavy oil, being also grateful to Mohamad Asrardel and Luis Ojeda for their assistance in several experimental tasks.

Appendix A. Supplementary data

Supplementary data to this article can be found online at https://doi.org/10.1016/j.energy.2024.133765.

Data availability

Data will be made available on request.

References

[1] Tariq AI, Saleh AM. An experimental investigation into the combustion properties, performance, emissions, and cost reduction of using heavy and light fuel oils. Case Stud Therm Eng 2023;44. https://doi.org/10.1016/j.csite.2023.102832.

[2] Tada K, Inoue K, Kawakami T, Saitoh K, Tanimura S. Expanding fuel flexibility in MHPS' dry low NOx combustor. In: Proceedings of ASME turbo expo 2018: turbomachinery technical conference and exposition. Oslo, Norway: ASME; 2018 Jun 11–15. https://doi.org/10.1115/gt2018-77164.

[3] Moldenhauer P, Rydén M, Mattisson T, Jamal A, Lyngfelt A. Chemical-looping combustion with heavy liquid fuels in a 10 kW pilot plant. Fuel Process Technol 2017;156:124–37. https://doi.org/10.1016/j.fuproc.2016.10.027.

[4] Jafarian M, Haseli P, Saxena S, Dally B. Emerging technologies for catalytic gasification of petroleum residue derived fuels for sustainable and cleaner fuel production—an overview. Energy Rep 2023;9:3248–72. https://doi.org/10.1016/j.egyr.2023.01.116.

[5] Lee S. Alternative fuels. first ed. New York: Routledge; 1996.

[6] Kokkinos NC, Emmanouilidou E, Sharma SK. Waste-to-biofuel production for the transportation sector. In: Upadhyay RK, Sharma SK, Kumar V, editors. Intelligent transportation system and advanced technology. Singapore: Springer Nature Singapore; 2024. p. 99–122.

[7] Wang ZW, Yuan B, Huang YH, Cao JH, Wang YZ, Cheng XB. Progress in experimental investigations on evaporation characteristics of a fuel droplet. Fuel Process Technol 2022;231. https://doi.org/10.1016/j.fuproc.2022.107243.

[8] Ballester JM, Dopazo C. Experimental study of the influence of atomization characteristics on the combustion of heavy oil. Combust Sci Technol 1994;103(1–6):235–63. https://doi.org/10.1080/00102209408907697.

[9] Bartle KD, Jones JM, Lea-Langton AR, Pourkashanian M, Ross AB, Thillaimuthu JS, et al. The combustion of droplets of high-asphaltene heavy oils. Fuel 2013;103:835–42. https://doi.org/10.1016/j.fuel.2012.07.004.

[10] Fasih HF, Ghassemi H, MazraeShahi HK. Experimental investigation of heavy fuel oil gasification in an entrained flow gasifier. Fuel 2023;351. https://doi.org/10.1016/j.fuel.2023.128955.

[11] Marrone NJ, Kennedy IM, Dryer FL. Coke Formation in the combustion of isolated heavy oil droplets. Combust Sci Technol 1984;36(3–4):149–70. https://doi.org/10.1080/00102208408923731.

[12] Bomo N, Lahaye J, Prado G, Claus G. Formation of cenospheres during pyrolysis of residual fuel oils. Symp (Int) Combust. 1985;20(1):903–11. https://doi.org/10.1016/s0082-0784(85)80579-8.

[13] Urban DL, Dryer FL. New results on coke formation in the combustion of heavy-fuel droplets. Symp (Int) Combust. 1991;23(1):1437–43. https://doi.org/10.1016/s0082-0784(06)80411-x.

[14] Urban DL, Huey SPC, Dryer FL. Evaluation of the coke formation potential of residual fuel oils. Symp (Int) Combust. 1992;24(1):1357–64. https://doi.org/10.1016/s0082-0784(06)80158-x.

[15] Elbaz AM, Khateeb AA, Roberts WL. PM from the combustion of heavy fuel oils. Energy 2018;152:455–65. https://doi.org/10.1016/j.energy.2018.03.163.

[16] Jiang L, Elbaz AM, Guida P, Al-Noman SM, AlGhamdi IA, Saxena S, et al. Cenosphere Formation during single-droplet combustion of heavy fuel oil. Energy Fuels 2019;33(2):1570–81. https://doi.org/10.1021/acs.energyfuels.8b03632.

[17] Kobayasi K. An experimental study on the combustion of a fuel droplet. Symp (Int) Combust. 1955;5(1):141–8. https://doi.org/10.1016/s0082-0784(55)80021-5.

[18] Michael MI, El-Wakil MM. On the self ignition of hydrocarbon mixtures. Symp (Int) Combust. 1967;11(1):1027–35. https://doi.org/10.1016/s0082-0784(67)80229-7.

[19] Jacques MT, Jordan JB, Williams A, Hadley-Coates L. The combustion of water-in-oil emulsions and the influence of asphaltene content. Symp (Int) Combust. 1977;16(1):307–19. https://doi.org/10.1016/s0082-0784(77)80334-2.

[20] Lightman P, Street PJ. Single drop behaviour of heavy fuel oils and fuel oil fractions. J Inst Energy 1983;56:3–11.

[21] Villasenor R, Garcia F. An experimental study of the effects of asphaltenes on heavy fuel oil droplet combustion. Fuel 1999;78(8):933–44. https://doi.org/10.1016/s0016-2361(99)00010-1.

[22] Xu G, Ikegami M, Honma S, Ikeda K, Nagaishi H, Takeshita Y. Burning droplets of heavy oil residual blended with diesel light oil: characterization of burning steps. Combust Sci Technol 2002;174(2):115–45. https://doi.org/10.1080/714922711.

[23] Xu G, Ikegami M, Honma S, Ikeda K, Ma X, Nagaishi H. Burning droplets of heavy oil residual blended with diesel light oil: distinction of burning phases. Combust Sci Technol 2003;175(1):1–26. https://doi.org/10.1080/00102200302367.

[24] Ikegami M, Xu G, Ikeda K, Honma S, Nagaishi H, Dietrich DL, et al. Distinctive combustion stages of single heavy oil droplet under microgravity. Fuel 2003;82(3):293–304. https://doi.org/10.1016/S0016-2361(02)00257-0.

[25] Xu G, Ikegami M, Honma S, Ikeda K, Mao X, Nagaishi H. Burning droplets of heavy oil residual blended with diesel light oil: analysis of coke behaviors. Energy Fuels 2003;17(3):779–90. https://doi.org/10.1021/ef020197b.

[26] Ganji MJZ, Ghassemi H. Evaluation of the solid particle from heavy fuel oil and its formation trend. Powder Technol 2023;427. https://doi.org/10.1016/j.powtec.2023.118744.

[27] Klimenko A, Shlegel NE, Strizhak PA. Breakup of colliding droplets and particles produced by heavy fuel oil pyrolysis. Energy 2023;283. https://doi.org/10.1016/j.energy.2023.128480.

[28] Hottel HC, Williams GC, Simpson HC. Combustion of droplets of heavy liquid fuels. Symp (Int) Combust. 1955;5(1):101–29. https://doi.org/10.1016/s0082-0784(55)80018-5.

[29] Ballester JM, Fueyo N, Dopazo C. Combustion characteristics of heavy oil-water emulsions. Fuel 1996;75(6):695–705. https://doi.org/10.1016/0016-2361(95)00309-6.

[30] Ashizawa M, Hara S, Kidoguchi K, Inumaru J. Gasification characteristics of extra-heavy oil in a research-scale gasifier. Energy 2005;30(11–12):2194–205. https://doi.org/10.1016/j.energy.2004.08.023.

[31] Choi Y-C, Lee J-G, Yoon S-J, Park M-H. Experimental and theoretical study on the characteristics of vacuum residue gasification in an entrained-flow gasifier. Korean J Chem Eng 2007;24(1):60–6. https://doi.org/10.1007/s11814-007-5010-7.

[32] Vaezi M, Passandideh-Fard M, Moghiman M, Charmchi M. Gasification of heavy fuel oils: a thermochemical equilibrium approach. Fuel 2011;90(2):878–85. https://doi.org/10.1016/j.fuel.2010.10.011.

[33] Fasih HF, Ghassemi H, Shahi HKM. Gasification of a heavy fuel oil: a parametric study on energy and exergy analysis for different gasifying agents. Pet Chem 2021;61(2):162–71. https://doi.org/10.1134/S0965544121020055.

[34] Zahedian M, Mehrpooya M, Mousavi SH, Shahrooei K, Ganjali MR. Proposal and investigation of a novel process configuration for heavy fuel oil gasification and light hydrocarbon production. Arab J Sci Eng 2023. https://doi.org/10.1007/s13369-023-07953-z.

[35] Mallick D, Sharma SD, Kushwaha A, Brahma HS, Nath R, Bhowmik R. Chapter 4 - emerging commercial opportunities for conversion of waste to energy: aspect of gasification technology. In: Hussain CM, Singh S, Goswami L, editors. Waste-to-Energy approaches towards zero waste. Elsevier; 2022. p. 105–27.

[36] Asrardel M, Muelas Á, Poonawala T, Ballester J. Impact of heat transfer due to fiber conduction, radiation and convection on the interpretation of experiments with isolated droplets. Combust Flame 2024;263:113384. https://doi.org/10.1016/j.combustflame.2024.113384.

[37] Ballester J, García-Armingol T. Diagnostic techniques for the monitoring and control of practical flames. Prog Energy Combust Sci 2010;36(4):375–411. https://doi.org/10.1016/j.pecs.2009.11.005.

[38] Liberzon A, Gurka R, Ben-Gida H. OpenPIV - Matlab 2020. https://doi.org/10.6084/M9.FIGSHARE.12330536.

[39] Baert RSG. A mathematical-model for heavy fuel droplet vaporization and pyrolysis in a high-temperature inert-gas. Combust Sci Technol 1993;90(1–4):125–47. https://doi.org/10.1080/00102209308907607.

[40] Lawn CJ. Principles of combustion engineering for boilers. Orlando, FL: United States: Academic Press Inc.; 1987.

[41] Law CK, Chung SH, Srinivasan N. Gas-phase quasi-steadiness and fuel vapor accumulation effects in droplet burning. Combust Flame 1980;38:173–98. https://doi.org/10.1016/0010-2180(80)90049-8.

[42] Curl Jr H, O'Donnell K. Chemical and physical properties of refined petroleum products. Report number: NOAA Technical Memorandum ERL MESA-17, https://library.oarcloud.noaa.gov/noaa_documents.lib/OAR/ERL_MESA/TM_ERL_MESA/TM_ERL_MESA-17.pdf; 1977.

[43] Wang ZW, Yuan B, Cao JH, Huang YH, Cheng XB, Wang YZ, et al. A new shift mechanism for micro-explosion of water-diesel emulsion droplets at different ambient temperatures. Appl Energy 2022;323. https://doi.org/10.1016/j.apenergy.2022.119448.

[44] Chen XY, Xi X, Zhang LA, Wang ZX, Cui ZC, Long WQ. Experimental study on nucleation and micro-explosion characteristics of emulsified heavy fuel oil droplets at elevated temperatures during evaporation. Appl Therm Eng 2023;224. https://doi.org/10.1016/j.applthermaleng.2023.120114.

[45] Setyawan HY, Zhu M. Cenosphere Formation and combustion characteristics of single droplets of vacuum residual oils. Combust Sci Technol 2023:1–18. https://doi.org/10.1080/00102202.2023.2170750.

[46] Bridgwater AV. Review of fast pyrolysis of biomass and product upgrading. Biomass Bioenergy 2012;38:68–94. https://doi.org/10.1016/j.biombioe.2011.01.048.

[47] Xu G, Ikegami M, Honma S, Ikeda K, Nagaishi H, Dietrich DL, et al. Burning droplets composed of light cycle oil and diesel light oil. Energy Fuels 2002;16(2):366–78. https://doi.org/10.1021/ef010112r.

[48] Kwack EY, Shakkottai P, Massier PF, Back LH. Morphology of globules and cenospheres in heavy fuel oil burner experiments. J Eng Gas Turbines Power 1992;114(2):338–45. https://doi.org/10.1115/1.2906594.

[49] Ancheyta J, Centeno G, Trejo F, Marroquín G, García JA, Tenorio E, et al. Extraction and characterization of asphaltenes from different crude oils and solvents. Energy Fuels 2002;16(5):1121–7. https://doi.org/10.1021/ef010300h.

[50] Sun Y-d, Wang Z-z, Li M-l, Xiao S-y. Structure and composition of n-pentane and n-heptane asphaltene from different properties crude. J Fuel Chem Technol 2022;50(9):1155. https://doi.org/10.19906/j.cnki.JFCT.2022018.